

# Preliminary Design Procedure for Gas Turbine Topping Reverse-Flow Wave Rotors

Pezhman AKBARI<sup>1</sup> and Norbert MÜLLER<sup>2</sup>

<sup>1,2</sup> Department of Mechanical Engineering  
Michigan State University

2500 Engineering Building, East Lansing, Michigan 48824-1226, U.S.A.

Phone: 517-432-9139, FAX: 347-412-7848, E-mail: [akbari@egr.msu.edu](mailto:akbari@egr.msu.edu) and [mueller@egr.msu.edu](mailto:mueller@egr.msu.edu)

## ABSTRACT

This paper shows a preliminary design procedure for four-port reverse-flow wave rotors for implementation in gas turbine applications. First, a thermodynamic cycle analysis evaluates the performance improvement of a 30 kW microturbine by implementing various wave-rotor topping cycles. Five different advantageous implementation cases for a four-port wave rotor into the given baseline engine are considered. Advantages and disadvantages are outlined. The results obtained show that almost all the cases studied benefit from the wave-rotor-topping, but the highest gain is obtained for the case in which the topped engine operates with the same turbine inlet temperature and compressor pressure ratio as the baseline engine. Then, a one-dimensional analytical gas dynamic model of the high-pressure phase (charging zone) is employed to calculate flow characteristics inside the channels. Charts and explanations are presented for optimum design. Useful design parameters such as port widths and rotor size are determined by formulating traveling times of the waves inside the channels.

## NOMENCLATUR

$a$	Speed of sound	m/s	$\gamma$	Specific heat ratio
$C_p$	Specific heat	J/kgK	$\eta$	Efficiency
$L$	Length	m	$\Pi$	Pressure ratio
$L_{gas}$	Gas penetration length	m	$\rho$	density
$M$	Mach number		<b>Subscripts</b>	
$p$	Pressure	Pa	1	Fresh air
$PR_W$	Wave rotor compression ratio		2	Compressed air
$R$	Gas constant	J/kgK	3	Burned gas
$T$	Temperature	K	4	Exhaust gas
$u$	Flow speed	m/s	2'	Air after primary shock
$V$	Rotor speed	m/s	3'	Gas after reflected shock
$w$	Shock speed	m/s	t	Total
$w_{net}$	Specific cycle work	J/kg	S	Primary shock
$W$	Port width	m	R	Reflected shock
			T	Tuned condition

## INTRODUCTION

Wave rotors are a family of unsteady-flow devices mainly used to improve the performance of gas turbines and propulsion systems. Wave rotors do not use mechanical components such as pistons or vaned impellers to compress the fluid. Instead, the pressure rise is obtained by generating compression waves in appropriate geometries. It has been proved that for the same inlet and outlet Mach numbers, the pressure gain in time-dependent flow devices can be much higher than that obtained in steady flow devices (Weber, 1995, Akbari et al., 2003a).

The idea of using a wave-rotor topping cycle was first proposed by Claude Seippel of Brown Boveri Company (BBC) in Switzerland in 1942 (Seippel, 1946, Meyer, 1947). Now BBC is Asea Brown Boveri (ABB) and its pressure wave supercharger termed as the Compresx® has been used commercially for passenger car and heavy diesel engines (Mayer et al., 1989, Zehnder et al., 1989).

Since the early 1960s the General Electric Company (GE), GPC, and Rolls Royce were involved in the development of a prototype wave rotor for gas turbine propulsion applications (Taussig, 1984, Shreeve and Mathur, 1985). Mathematical Science Northwest (MSNW) also studied various aspects of wave energy exchange and proposed a wave rotor design for aircraft turbofan engines (Taussig, 1984). In the 1980s different U.S. agencies like DARPA (Defense Advanced Research Program Projects Agency) and the U.S. Navy expressed interest and sponsored programs to develop an understanding of wave rotor technology. Many developments were presented in the 1985 ONR/NAVAIR Wave Rotor Research and Technology Workshop (Shreeve and Mathur, 1985).

Interest in wave rotor technology has again increased recently. Since the 1990s, a large research program at NASA Glenn Research Center (GRC) collaborated by the U.S. Army Research Laboratory (ARL) and Rolls-Royce Allison has initiated to develop and demonstrate the benefits of the wave rotor technology, which will be useful in future aircraft propulsion designs. An excellent overview has been given by Welch (2000). Using a thermodynamic approach to calculate the thermal efficiency and specific power, a feasibility study for topping jet engines with a wave rotor was has been performed by Wilson and Paxson (1993). Applied to the case of an aircraft flying at Mach 0.8, they have shown that a wave-rotor topped engine may gain 1...2% in efficiency and 10...16% in specific power compared to a simple jet engine with the same overall pressure ratio and turbine inlet temperature. Paxson also developed a one-dimensional design model to calculate off-design wave rotor performance and verified it using experimental data (Paxson, 1993). The model solves the unsteady viscous flow field in an axial passage for time-constant inlet and outlet port conditions,

while accounting for losses due to gradual passage opening and closing, viscous and heat transfer effects, leakage, and non-uniform port flow field mixing. Recent improvement and validations have completed it as a preliminary and general design tool. However, simpler computational tools would be beneficial for wide industrial use. Welch et al. (1995) used this model and predicted in performance calculations for small (300 to 500 kW) and intermediate (2000 to 3000 kW) wave-rotor-enhanced turboshaft engines a 19...21% increase in specific power and a 16...17% decrease in specific fuel consumption compared with the baseline engines. Same calculations for a wave-rotor-enhanced large turbofan engine, equal in thrust to the baseline engine, have shown a 6...7% reduction in trust specific fuel consumption. Welch also has established one-dimensional and two-dimensional analysis models to estimate the performance enhancements of wave rotors (Welch et al., 1993, Welch, 1996a, 1996b, 1997a, 1997b).

Snyder and Fish have evaluated the Rolls-Royce Allison 250 turboshaft engine as a potential platform for a wave rotor demonstration, predicting a 18...20% increase in specific power and a 15...22% decrease in specific fuel consumption (Snyder, 1996, Snyder and Fish, 1996, Welch, 2000). They used a detailed map of the wave rotor cycle performance accomplished by Wilson and Paxson (1993, 1996). After a numerical modeling performed by Fatsis and Ribaud (1997, 1998) from the French National Aerospace Research Establishment (ONERA), they carried out a basic investigation of the thermodynamic performance enhancement for various types of gas turbines topped with wave rotors, including auxiliary power units, turboshaft, turbojet, turbofan (Fatsis and Ribaud, 1999). The variation of wave-rotor compression and expansion efficiency, as well as mixing and pressure losses in the ducting, have been taken into account. The results have shown the largest gains in power and largest reduction of specific fuel consumption for engines with a low compressor pressure ratio and high turbine inlet temperature, such as turboshaft engines and auxiliary power units. These results have been consistent with those obtained by Jones and Welch (1996) for the wave-rotor topping of turboshaft, high-bypass turbofan, auxiliary power, and ground based power engines.

While numerical and experimental analyses of enhancing gas turbines by wave rotors have been performed extensively as discussed above, much less has been documented about a detailed and complete analytical design method itself. The present work introduces a design procedure for a four-port reverse-flow wave rotor topping a gas turbine which will be useful for preliminary design studies and has not been published before. The procedure is divided in two sections: thermodynamic cycle analysis and gas dynamic analysis within the rotor channels. The first is also applicable for through-flow (TF) wave rotors, whereas the latter is restricted to reverse-flow wave rotors. In contrast to using existing computational tools for determining the performance, the presented results were obtained using basic thermodynamic equations along with the wave-rotor characteristic equation introduced by Wilson and Paxson (1993). The gas dynamic analysis is a straightforward procedure employing existing normal shock wave equations along with isentropic relations for expansion waves. The work shows that there is a strong link between the external thermodynamics and the internal wave cycle. This is complemented with optimum design considerations.

### WAVE ROTOR ENHANCED-CYCLES

Two basic wave rotor cycles termed as four-port through-flow (TF) and four-port reverse-flow (RF) cycles can be considered. They may provide identical topping and overall performance enhancement, but they differ substantially in their internal process.

The four-port TF wave rotor is often used to top gas turbine engine as illustrated in Fig. 1. The internal process can briefly be described as follows: In the wave rotor channels, the hot gas leaving the combustion chamber compresses the air coming out of the compressor. This means that wave rotors utilize a high-pressure

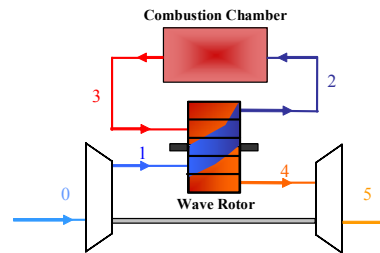


Fig. 1 Schematic of a gas turbine cycle topped by a four-port through-flow (TF) wave rotor

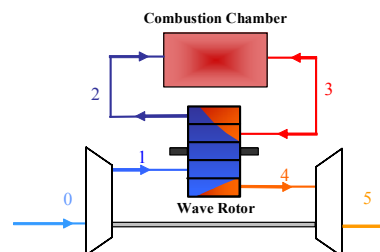


Fig. 2 Schematic of a gas turbine cycle topped by a four-port reverse-flow (RF) wave rotor

fluid to transfer its energy directly to a low-pressure fluid. After the additional compression of the air in the wave rotor, it is discharged into the combustion chamber. The pre-expanded burned gas is then scavenged toward the turbine and the channels are re-connected to the compressor outlet, allowing fresh pre-compressed air to flow into the wave rotor channels. The pre-expanded gas entering the turbine from the wave rotor can have the same temperature as the gas would have in a conventional arrangement without the wave rotor. However, the gas pressure is higher than the compressor exit pressure by the pressure gain obtained in the wave rotor. This is the advantageous difference to the untopped engine, where - by the pressure loss occurring in the combustion chamber - the turbine inlet pressure is lower than the compressor discharge pressure. Details of the internal processes inside the rotor channels will be explained later in the gas dynamic section of this work.

In the TF configuration, for both gas and air, the inlet ports are located on one side of the rotor and the outlet ports are located on the other side of the rotor. Thus, the hot gas and in particular the relatively cold air route through the full length of the rotor leading to the self-cooling feature, which is essential for very high gas temperatures in gas turbine applications. However detailed fluid flow investigations have suggested that approximately 30 to 50 percent of burned gas is recirculated to the combustion chamber in TF configuration (Welch et al., 1997).

The operation of a four-port RF wave rotor is very similar to that of a TF wave rotor. However, the fresh air enters and exits at the same end of the rotor (air casing), as shown in the Fig. 2, while the burned gas enters and exits the rotor at the other end (gas casing). Hence, the RF cycle does not inherently result in such a well self-cooled rotor. The cold air never reaches the other side of the rotor, which is also true for the hot gas. Thus, the air side of the rotor is relatively cool, while the gas side of the rotor is relatively hot. To achieve a better self-cooled RF design, a two cycle per revolution design of the RF configuration can be constructed, which orients the cycle alternately right and left on the rotor (Snyder, 1996). This approach introduces symmetry and assures that both sides of the rotor are washed by the relatively cold fresh air. Unfortunately, it also poses severe ducting challenges. However, for small gas turbines, gas temperatures are often lower. Then the RF approach seems to be the viable choice. Also, it has been claimed that the RF cycle provides better separation of air and gas in the rotor channels (Weber, 1995). Due to this separation of air and gas regions in the channels, the analytical analysis of the fluid flow inside RF wave rotor channels is easier.

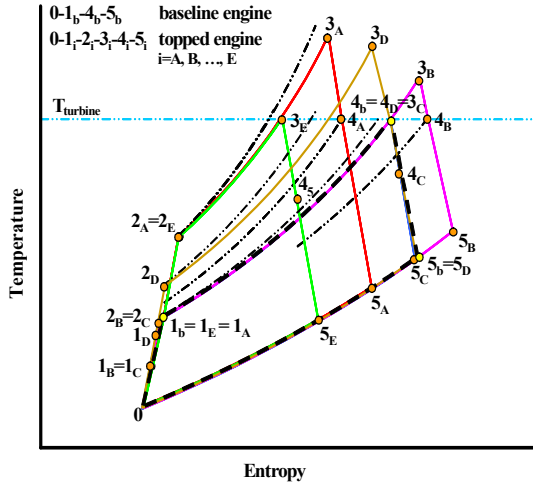


Fig. 3 Schematic Temperature-Entropy diagram for a baseline cycle and five different wave-rotor-topped cycles

### THERMODYNAMIC ANALYSIS

With some modifications, the methodology is similar to the one introduced by Wilson and Paxson (1993), using the wave-rotor characteristic equation:

$$\frac{P_{t4}}{P_{t1}} = \Pi_{comb} PR_W \left\{ 1 - \frac{\frac{C_{p_{air}}}{C_{p_{gas}}} \frac{1}{\eta_{WE} \eta_{WC}} \frac{T_{t1}}{T_{t4}} \left[ PR_W^{(\gamma_{air}-1)/\gamma_{air}-1} \right]^{\gamma_{gas}/\gamma_{gas}-1}}{1 + \frac{C_{p_{air}}}{C_{p_{gas}}} \frac{1}{\eta_{WC}} \frac{T_{t1}}{T_{t4}} \left[ PR_W^{(\gamma_{air}-1)/\gamma_{air}-1} \right]} \right\} \quad (1)$$

To evaluate the theoretic performance enhancement of a wave-rotor-topped gas turbine, the specific cycle work  $w_{net}$  and overall thermal efficiency  $\eta$  are calculated for the wave-rotor-topped and the baseline engine:

$$w_{net} = \eta_T C_{p_{gas}} T_{t4} \left[ 1 - \left( \frac{P_{t0}}{P_{t4}} \right)^{\frac{\gamma_{gas}-1}{\gamma_{gas}}} \right] - \frac{C_{p_{air}} T_{t0}}{\eta_C} \left( R^{\frac{\gamma_{air}-1}{\gamma_{air}}} - 1 \right) \quad (2)$$

$$\eta = \frac{\eta_Q w_{net}}{C_{p_{gas}} T_{t4} - C_{p_{air}} T_{t1}} \quad (3)$$

Since the rotor has zero net work output, the highest cycle temperature for the topped engine ( $T_{t3}$ ) can be calculated by equating the wave rotor compression work to the wave rotor expansion work:

$$T_{t3} = T_{t4} + \left[ \frac{T_{t1}}{\eta_{WC}} \left( PR_W^{\frac{\gamma_{air}-1}{\gamma_{air}}} - 1 \right) \right] \frac{C_{p_{air}}}{C_{p_{gas}}} \quad (4)$$

In the calculations, it is assumed that the compressor inlet condition is known and is the same for both the baseline engine and the wave-rotor-enhanced engine. The considered 30 kW microturbine baseline engine here has a compression ratio of  $p_{t1}/p_{t0}=3.6$ . The compressor and turbine isentropic efficiencies are  $\eta_C=79.6\%$  and  $\eta_T=84.0\%$  respectively. Considering the same "aerodynamic quality" of the wheels, the polytropic efficiencies are kept the same for the enhanced and baseline engine, for the compressor ( $\eta_{pC}=82.9\%$ ) and turbine ( $\eta_{pT}=81.7\%$ ) respectively. Incomplete combustion of the fuel is reflected by a combustor efficiency of  $\eta_Q=98.0\%$ . Further, a 2.0% pressure drop in the

combustor is considered by  $\Pi_{comb}=0.98$ . The fuel mass addition is ignored. No pressure losses in intake air filter, exhaust silencer and additional piping, or heat losses, or mechanical losses are considered here. Such losses will reduce the predicted performance. The gases are treated as ideal gases with constant values for specific heat coefficients ( $C_{p_{air}}=1.005$  kJ/kgK,  $C_{p_{gas}}=1.148$  kJ/kgK) and the ratio of specific heats ( $\gamma_{air}=1.4$ ,  $\gamma_{gas}=1.33$ ). Air is entering the compressor at 101.3 kPa and 300 K. The maximum allowable turbine inlet temperature is set to  $T_{t4} \leq 1116.5$  K. According to previous wave rotor investigations (Wilson and Paxson, 1993, Welch, 1996b, Fatsis and Ribaud, 1999), the wave rotor compression and expansion efficiencies are assumed with  $\eta_{WC}=\eta_{WE}=0.83$ . A wave rotor compression ratio of  $PR_W=p_{t2}/p_{t1}=1.8$  representing the ratio of the total pressure across the wave rotor appears to be conceivable for the envisioned application and is chosen for the discussion of representative values. However, in this work the plots are shown for various wave rotor pressure ratios indicating its effect on the performance enhancement.

### Implementation Cases

There are several wave-rotor topping cycles that may be suited for a gas turbine application. Knowing about possible design restrictions and preferences, when an existing gas turbine is to be enhanced, mainly five different advantageous implementation cases for a wave rotor into given baseline engines can be introduced as the following:

- Case A:** same compressor, same turbine inlet temperature
- Case B:** same overall pressure ratio, same turbine inlet temperature
- Case C:** same combustor
- Case D:** same turbine
- Case E:** same compressor, same combustion end temperature

Figure 3 visualizes all five cases in a schematic T-s diagram. Path 0-1<sub>b</sub>-4<sub>b</sub>-5<sub>b</sub> represents the baseline cycle and 0-1<sub>i</sub>-2<sub>i</sub>-3<sub>i</sub>-4<sub>i</sub>-5<sub>i</sub> with index  $i=A, B, \dots, E$  indicates the various wave-rotor-topped cycles. One of the five cases might be preferred for a practical design. However intermediate design cases are possible too.

In Case A (0-1<sub>A</sub>-2<sub>A</sub>-3<sub>A</sub>-4<sub>A</sub>-5<sub>A</sub>) the pressure ratio of the compressor is kept unchanged, so the physical compressor of the baseline engine can also be used for the wave-rotor-enhanced engine, provided the mass flow is kept approximately the same. The pressure in the combustion chamber of the enhanced engine is increased by the wave-rotor compression ratio ( $1.8 \times 3.6 = 6.48$ ) and the turbine inlet pressure is higher. The turbine inlet temperature, however, is the same as it is for the baseline engine. The thermal efficiency is higher, because the turbine produces more specific work, while consumption of specific work by the compressor and specific heat addition to the cycle are the same as for the baseline engine. This implementation case gives the highest performance increase for the baseline engine and is commonly discussed in the literature.

In Case B (0-1<sub>B</sub>-2<sub>B</sub>-3<sub>B</sub>-4<sub>B</sub>-5<sub>B</sub>) the overall pressure ratio for the wave-rotor-enhanced engine is kept equal to that of the baseline engine, so that the combustor works under the same pressure. However, for the wave-rotor-topped engine, the heat addition in the combustor and the combustion end temperature are higher than those of the baseline engine. For both the turbine and the compressor, the required pressure ratios are less. This case not only demonstrates an attractive performance enhancement, additionally it provides the highest turbine outlet temperature. Therefore this case is especially attractive for an external heat recovery application or for internal recuperation enhancing the performance even more.

Case C (0-1<sub>C</sub>-2<sub>C</sub>-3<sub>C</sub>-4<sub>C</sub>-5<sub>C</sub>) keeps the overall pressure ratio and also the combustor inlet and outlet temperature of the wave-rotor-enhanced engine equal to those of the baseline engine. This reduces the pressure ratios of compressor and turbine and the turbine inlet temperature.

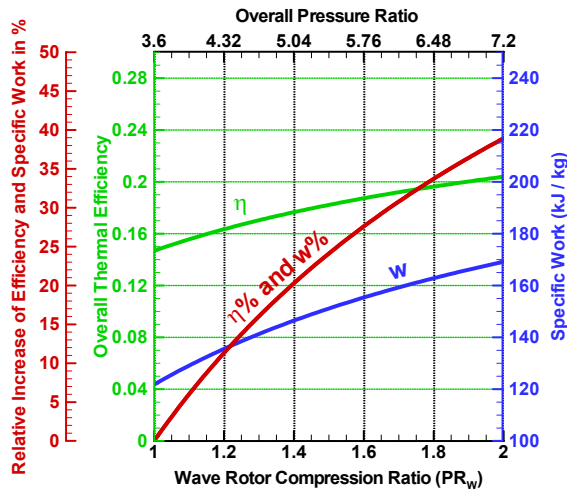


Fig. 4 Overall thermal efficiency and specific work of the wave-rotor-topped engines versus wave rotor pressure ratio and overall pressure ratio (Case A)

Case D (0-1<sub>D</sub>-2<sub>D</sub>-3<sub>D</sub>-4<sub>D</sub>-5<sub>D</sub>) employs the same physical turbine as the baseline engine instead of the same compressor in Case A. The pressure in the combustion chamber is higher than that for the baseline engine but lower than it would be in Case A.

Case E (0-1<sub>E</sub>-2<sub>E</sub>-3<sub>E</sub>-4<sub>E</sub>-5<sub>E</sub>) is similar to Case A but the combustion end temperature - the maximum cycle temperature - is restricted to the turbine inlet temperature of the baseline engine, in order to not impose additional thermal requirements for the combustor. This reduces the turbine inlet temperature substantially. The overall pressure ratio is the same as in Case A.

#### Predicted Performance Results

Comparisons between the above cases as well as advantages and disadvantages of each case are extensively discussed by Akbari and Müller (2003b). The results of their studies indicate a 33.6%, 6.2%, 1.5%, 24.5%, and 22.6% relative increase in the overall thermal efficiency for each case respectively and correspondingly a relative increase in the specific shaft work of 33.6%, 17.3%, 1.7%, 30.1%, and 7.1% for each case.

Figure 4 illustrates the increase of cycle overall thermal efficiency (green) and specific work (blue) with increases of values of the wave rotor pressure ratio  $PR_w$  for Case A. The plot visualizes how the effect develops from the baseline engine with  $PR_w=1$  until  $PR_w=2$ , which might be a practical upper limit for the investigated application. However, if the wave rotor pressure ratio increases beyond this limit the trend shows that the increasing effect becomes less, while technical problems may increase. With a conceivable wave rotor pressure ratio of 1.8, the overall thermal efficiency of the baseline cycle increases from 14.7% to 19.6% for the enhanced engine. Simultaneously, the specific work increases from 122 kJ/kg to 163 kJ/kg. This means an attractive relative performance improvement in overall thermal efficiency and specific work (red line in Fig. 4) of about 33.6%.

Figure 5 shows a map of the relevant design space, which allows predicting the performance of the wave-rotor-enhanced engine in terms of overall efficiency (green) and specific work (blue) for any combination of compressor pressure ratio (abscissa) and wave rotor pressure ratio  $PR_w$  (parameter labeled in black). In this map, the multiplication of compressor pressure ratio  $p_{t1}/p_0$  and wave rotor pressure ratio  $PR_w$  determines the overall cycle pressure ratio  $p_{t2}/p_0$  (red). The optimum compressor pressure ratio points for highest overall efficiency and specific work at each achievable wave rotor pressure ratio are connected by black solid lines.

This performance map is general. The only specific parameters are indicated in the upper right corner of the map. They are mainly turbine inlet temperature and polytropic efficiencies of compressor and turbine, which correspond to the baseline engine. Such a map is

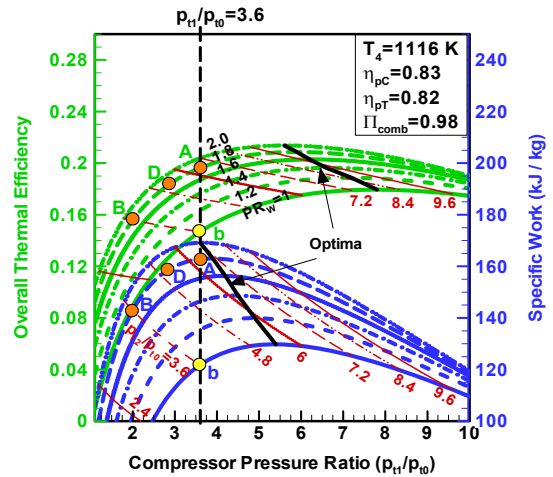


Fig. 5 Maps of overall thermal efficiency and specific work for wave-rotor-topping of gas turbines

not only useful to explore the possible enhancement of already existing baseline engines, but it also serves very well for selecting a design point or region when designing a new wave-rotor-topped engine.

In the performance map, points for overall thermal efficiency and specific work of the baseline engine and the wave-rotor-enhanced engines of Case A, B and D ( $PR_w=1.8$ ) are indicated. Starting from the performance point of the baseline engine, the performance values for Case A are found by moving vertically upwards (along a line for constant compressor pressure ratio  $p_{t1}/p_0$ ) until the corresponding performance curve of the expected wave rotor pressure ratio is crossed. Case B is found by moving along a line for constant overall pressure ratio  $p_{t2}/p_0$ . Case D actually lies on a line for constant turbine pressure ratio (not shown). Case C and E can not be shown in the same map, since in both cases the turbine inlet temperature is less than indicated in the upper right corner of the map.

The results indicate that for every compressor pressure ratio in the shown design space, the performance of the topped engine is always higher than that of the corresponding baseline engine with the same compressor pressure ratio (Case A consideration). However, for higher compressor pressure ratios, less benefit can be obtained by using a wave rotor. In other words, the benefit is the greatest for lower compressor pressure ratios. This clearly favors the wave-rotor topping for small gas turbines with low compressor pressure ratios such as microturbines.

#### GAS DYNAMIC ANALYSIS

In this section, one-dimensional analytical gas dynamic models are used to analyze the high-pressure phase of a four-port RF wave rotor. The methodology is similar to that used by Keller (1984). The following assumptions are made for the analysis. In the rotor, the flow itself is considered to be frictionless, adiabatic, and one-dimensional. However, the wave rotor efficiency is used to account for dissipation losses inside the channels. The gases are treated as ideal gases. Expansion waves are represented as thin waves. Furthermore, it is assumed that pressure equalization occurs faster than mixing. Thus, the thickness of the mixing layer between the burned gas and the fresh air inside the channels is negligible small and mixing between the gases is ignored. The fuel mass addition is again neglected.

Figure 6 shows the wave diagram of the charging zone with the channels moving in upward direction. The wave diagram describes the wave processes and the cycle in the rotor by tracing the trajectories of the waves and gas interfaces, which determines the cycle timing (ports opening and closing).

The burned gas coming from the combustor enters the rotor

through the inlet port 3. The air, compressed by the hot gas, leaves the channels through the outlet port 2. The ducts are set at the correct angle, so that in the rotor reference frame the flow can enter and leave the rotor aligned with its axis. The shock wave trajectory is shown by a dashed line. Expansion waves (fans) are depicted by thin solid lines. The trajectory of the air/gas interface is indicated by a dotted line.

The process begins in the bottom part of Fig. 6, where the channel is closed at both ends and contains fresh air only (region 1). By further rotation, the channel is exposed to the exhaust gas arriving from the combustion chamber. The hot burned gas begins to penetrate into the channel (region 3). Since the pressure of it is higher than the pressure of the fresh air, a shock wave is triggered from the lower corner of the inlet duct. It runs through the channel and causes an abrupt rise of local pressure inside the channel. The shock wave speed is higher than the local speed of sound. Within the relevant design space the flow speeds are everywhere subsonic. Therefore, the air/gas interface follows the shock wave with an induced velocity  $u_{2'}$  which is less than the speed of sound. Behind the shock wave (region 2'), the compressed air has the same local pressure and speed as the inlet exhaust gas ( $p_{2'} = p_3$  and  $u_{2'} = u_3$ ). As the shock wave reaches the end of the channel, the outlet port 2 is opened through which the compressed air is then pushed to the combustion chamber. This is usually called the tuning condition for the primary shock wave (Croes, 1978, Gyarmathy, 1983, Keller, 1984, Oberhem and Nour Eldin, 1995). In the following it is referred to as Tuning Condition 1 (TC 1). At this moment, the gas and the compressed air column in the channel have the same local pressure and move uniformly with the same induced velocity toward the outlet port. Due to TC 1, a reflected shock wave is originated at lower outlet edge and propagates from the right to the left with velocity  $w_{R-air}$  into the part of the channel that contains air flowing with velocity  $u_{2'}$  from left to right. The double-compressed air behind the reflected shock wave, leaving the wave rotor toward the combustion chamber, is region 2. In Fig. 6,  $L_s$  represents the location where the reflected shock wave intersects the air/gas interface. After crossing the air/gas interface, the velocity of the reflected shock wave increases from  $w_{R-air}$  to  $w_{R-gas}$ , where the later is the velocity of reflected shock wave in the gas region 3. The increase in the velocity is mainly due to the fact that the burned gas has a higher temperature than the compressed air. The compressed gas region behind the reflected shock wave is region 3'. The reflected shock wave reduces the speed of the flow leaving the channel from  $u_{2'}$  to  $u_2$  and causes a further local pressure rise within the channel from  $p_{2'}$  to  $p_2$ . Here, a favorite case is considered where the closure of the gas inlet port is timed with the arrival of the reflected shock wave. This is called the tuning condition 2 (Croes, 1978, Gyarmathy, 1983, Oberhem, and Nour Eldin, 1995), here denoted by TC 2. This way, all the fluid column in the channel is compressed by the reflected shock allowing more gas to enter the channel.

By closing the gas inlet port, an expansion wave originates from the upper corner of the inlet port and propagates toward the right end of the channel. Since this expansion wave induces a flow velocity equal but opposite to that of the gas flow, the gas flow behind this expansion wave is stopped and its local pressure is decreased. Both local and total pressure behind the expansion wave are still considerably higher than the pressure of the fresh air in the beginning of the process. Since the expansion wave is traveling faster than the air/gas interface, it overtakes the air/gas interface before the latter reaches the right end of the channel. In Fig. 6,  $L_{gas}$  denotes the location where the first disturbance of the expansion wave catches the air/gas interface.

Tuning condition 3 (TC 3) is fulfilled if the expansion wave reaches the end of the channel at the moment when the upper edge of the outlet port closes the channel (Croes, 1978, Gyarmathy, 1983, Keller, 1984, Oberhem, and Nour Eldin, 1995). It is highly possible that for a given  $PR_W$ , TC 3 might not be achieved (Akbari and

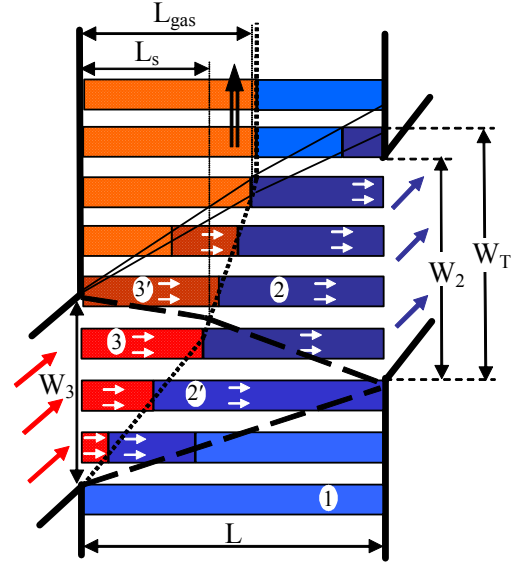


Fig. 6 Wave Diagram of high-pressure part

Müller, 2003c). Then, another shock wave would originate from the upper corner of the outlet port in order to satisfy zero-slip boundary condition at the end wall. This is undesirable and not shown in Fig. 6, although it describes a general case where TC 3 is not fulfilled.  $W_3$  and  $W_2$  are the inlet and outlet port width, respectively.  $W_T$  is the outlet port width at which the tuning condition TC 3 is fulfilled. When the expansion wave reaches the end of the channel, the trapped flow within the channel consists of a large part of the hot gas and a plug of compressed air preventing the hot gas to contact the end wall. Thus, during the high-pressure process penetration of the hot gas into the outlet flow is completely avoided.

For a detailed analysis, the following dimensionless quantities called flow Mach number, primary shock Mach number, inlet gas Mach number, and induced Mach number of the air are defined as:

$$M = \frac{u_{2'}}{a_1}, \quad M_s = \frac{w_s}{a_1}, \quad M_3 = \frac{u_{2'}}{a_3}, \quad M_{2'} = \frac{u_{2'}}{a_{2'}} \quad (5)$$

where  $w_s$  denotes the speed of the primary shock wave, and  $a_1$  and  $a_{2'}$  represent the speed of sound respectively in region 1 (fresh air) and in region 2' (compressed air region behind the primary shock wave).  $a_3$  is the speed of sound in gas region 3. Using the normal shock wave equations across the primary shock wave, the Hugoniot equation, and the perfect gas relation, the above dimensionless quantities can be calculated as function of the local pressure ratio across the primary shock wave introduced by  $\Pi_s = p_2/p_1$  (Akbari and Müller, 2003c).

Beginning with the inlet gas port, the ratio of the total to local temperature of the burned gas entering the channels can be written as:

$$\frac{T_{i3}}{T_3} = 1 + \frac{\gamma_{gas} - 1}{2} \left( \frac{\sqrt{u_{2'}^2 + V^2}}{a_3} \right)^2 \approx 1 + \frac{\gamma_{gas} - 1}{2} \left( \frac{u_{2'}^2}{a_3^2} \right) = 1 + \frac{\gamma_{gas} - 1}{2} M_3^2 \quad (6)$$

where  $V$  stands for the radially averaged rotor speed. The velocity of the flow in the inlet duct is  $(u_{2'}^2 + V^2)^{1/2}$ . However, it has been justified that the rotor speed is small compared to the flow sound speeds, i.e.  $V \ll a_3$ . Therefore,  $V$  has been omitted in the right side of Eq. (6) (Keller, 1984). The value of  $T_{i3}$  can be obtained by combining Eq. (6) and the local temperature ratio across the air/gas interface calculated by:

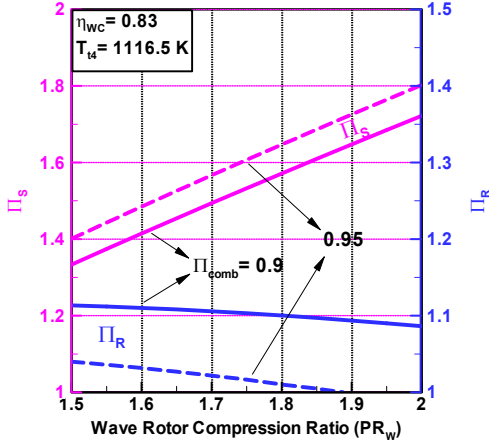


Fig. 7 Variation of  $\Pi_S$  and  $\Pi_R$  versus  $PR_W$  for two different values of  $\Pi_{comb}$

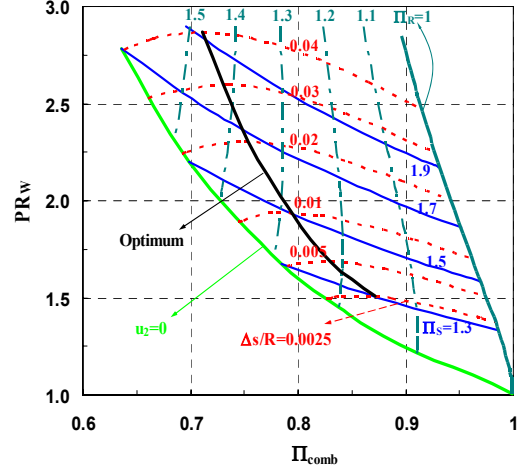


Fig. 8 Shock strength  $\Pi_S$ ,  $\Pi_R$  and entropy production  $\Delta s/R$  versus  $PR_W$  and  $\Pi_{comb}$

$$T_{13} = \frac{T_3}{T_2} T_2 \left( 1 + \frac{\gamma_{gas} - 1}{2} M_3^2 \right) = \frac{\gamma_{air} R_{air}}{\gamma_{gas} R_{gas}} \left( \frac{M_2'}{M_3} \right)^2 T_2 \left( 1 + \frac{\gamma_{gas} - 1}{2} M_3^2 \right) \quad (7)$$

It was already shown that  $T_{13}$  also can be obtained by Eq. (4).

The external pressure balance gives Eq. (8). It relates the local pressure ratio across the primary shock wave  $\Pi_S$  to the given  $PR_W$  and the pressure ratio in the combustor  $\Pi_{comb}$ . In the thermodynamic section  $\Pi_{comb} = 0.98$  was fixed. Here,  $\Pi_{comb}$  may be adjusted to obtain a different value of  $\Pi_S$  as it will be discussed further below.

$$\Pi_{comb} PR_W \approx \left[ 1 + \frac{\gamma_{gas} - 1}{2} M_3^2 \right]^{\frac{\gamma_{gas}}{\gamma_{gas} - 1}} \cdot \Pi_S \quad (8)$$

Simultaneously solving Eq. (4, 7, and 8) along with the normal shock wave equations calculates  $\Pi_S$  for given  $PR_W$  and  $\Pi_{comb}$ .

In order to find quantities across the reflected shock wave, it is convenient to define the Mach number of the reflected shock in the air region as:

$$M_{R-air} = \frac{w_{R-air} + u_2'}{a_2} \quad (9)$$

Normal shock wave equations across the reflected shock give:

$$M_{R-air} = \sqrt{\frac{\gamma_{air} + 1}{2\gamma_{air}} (\Pi_R - 1) + 1} \quad (10)$$

where  $\Pi_R = p_2/p_2'$  is the local pressure ratio across the reflected shock wave. The exit Mach number  $M_2 = u_2/a_2$  can be obtained by using continuity and momentum equations:

$$M_2 = \left[ \frac{u_2'}{a_2} - \frac{2}{\gamma_{air} + 1} \left( \frac{M_{R-air}^2 - 1}{M_{R-air}} \right) \right] \sqrt{\frac{T_2'}{T_2}} \quad (11)$$

Because  $u_2'$  and  $a_2'$  are functions of  $\Pi_S$ , and  $M_{R-air}$ , and  $T_2'/T_2$  is a function of  $\Pi_R$ , the exit Mach number  $M_2$  relates  $\Pi_S$  to  $\Pi_R$ . The internal pressure balance gives:

$$PR_W = \frac{p_{12}}{p_{11}} = \frac{p_{12}}{p_2} \frac{p_2}{p_2'} \frac{p_2'}{p_1} \approx \left[ 1 + \frac{\gamma_{air} - 1}{2} M_2^2 \right]^{\frac{\gamma_{air}}{\gamma_{air} - 1}} \Pi_R \Pi_S \quad (12)$$

Simultaneously solving Eq. (9-12) calculates  $\Pi_R$  for a given  $PR_W$

and the above determined  $\Pi_S$ . Figure 7 visualizes the variation of  $\Pi_S$  and  $\Pi_R$  versus  $PR_W$  for constant  $\Pi_{comb}$ .

A general map relating the shock strength  $\Pi_S$  and  $\Pi_R$  to various combinations of  $PR_W$  and  $\Pi_{comb}$  is provided in Fig. 8. The right boundary of the map is the  $\Pi_R = 1$  line, where the reflected shock wave vanishes. The lower and left boundary is the  $u_2 = 0$  line, simulating the closed wall condition where no flow leaves the channel anymore. This condition occurs when  $\Pi_R$  approaches the value of  $\Pi_S$ . The most interesting in the map are the lines of constant entropy production in the channels due to the shock waves. The entropy production  $\Delta s$  is calculated by summation of entropy generations across primary and reflected shock waves. They have been normalized by gas constants of the air and gas, respectively. For a desired fixed  $PR_W$ , coming from the  $\Pi_R = 1$  line with only a primary shock,  $\Delta s/R$  becomes less as the reflected shock  $\Pi_R$  becomes stronger. This shows the potential for higher efficiency, if the wave rotor is designed with a reflected shock wave. However, this continues only until the optimum line (solid black) is reached. The optimum line indicates the combinations of  $PR_W$  and  $\Pi_{comb}$  at which the least entropy production occurs in the charging zone for a given  $PR_W$ . Left of it, the entropy production increases again for a given  $PR_W$ . Simultaneously in Fig. 8 from the right to the left,  $\Pi_{comb}$  decreases. This allows for a combustor with a higher pressure drop that may be smaller and more compact, which is especially desired for aerospace applications. In fact, Fig. 8 shows that for the desired  $PR_W = 1.8$ , the value of  $\Pi_{comb} = 0.98$  considered in the thermodynamic analysis gives an impossible value of  $\Pi_R < 1$ . Thus, a higher pressure drop ( $\Pi_{comb} < 0.98$ ) must be selected for the proposed wave rotor, which may preferably reduce its size.

For an actual design of a wave rotor, the ratio of outlet port to the inlet port width ( $W_2/W_3$ ) is used to determine the port widths. Using the continuity equation between the inlet and outlet ports, neglecting the small amount of fuel addition, and some algebra using normal shock equations across the primary and reflected shock waves, the following equation can be obtained (Akbari and Müller, 2003c):

$$\left\{ 1 - \left( \frac{T_2'}{T_3} \frac{R_{air}}{R_{gas}} \right) \left( \frac{\gamma_{air} + 1}{\gamma_{air} - 1} + \Pi_R \right) \left( \frac{W_2}{W_3} \right)^{-1} \right\} u_2' = \left( \frac{a_2'}{\gamma_{air}} \right) \frac{\Pi_R - 1}{\sqrt{\frac{\gamma_{air} + 1}{2\gamma_{air}} (\Pi_R - 1) + 1}} \quad (13)$$

where  $u_2'$ ,  $a_2'$ ,  $T_2'/T_3$  are functions of  $\Pi_S$ . Thus, this equation implicitly relates  $W_2/W_3$  to  $\Pi_S$  and  $\Pi_R$ , which have been already determined previously for given  $PR_W$  and  $\Pi_{comb}$ .

The location where the air/gas interface meets the reflected shock wave ( $L_s$ ) can be found by equating the time required for the

air/gas interface originated from the lower corner of the inlet port to reach the reflected shock wave ( $L_S/u_2'$ ) with the time required for the primary shock wave to run through the channel ( $L/w_S$ ) plus the time for the reflected shock wave to meet the air/gas interface ( $(L-L_S)/w_{R-air}$ ):

$$\frac{L_S}{L} = \frac{\frac{1}{M_S} + \frac{1}{w_{R-air}/a_1}}{\frac{1}{M} + \frac{1}{w_{R-air}/a_1}} \quad (14)$$

The penetration length for the charging zone with reflected shock wave (nearly exact  $L_{gas}$ ) can be calculated by equating the time required for the air/gas interface to be overtaken by the expansion wave with the opening time of the inlet port plus the time required for the expansion wave to catch the air/gas interface:

$$\frac{L_{gas}}{L} = \frac{\frac{L_S}{L} \left( \frac{1}{M} - \frac{1}{u_2/a_1} \right) - \frac{W_3}{M_R L}}{\frac{1}{(u_2 + a_3)/a_1} - \frac{1}{u_2/a_1}} \quad (15)$$

where  $M_R$  is the rotor Mach number defined as  $M_R = V/a_1$ . The value of  $W_3/M_R/L$  can be obtained from TC 2:

$$\frac{W_3}{M_R L} = \frac{1}{M_S} + \frac{1}{w_{R-air}/a_1} + \left( \frac{1}{w_{R-gas}/a_1} - \frac{1}{w_{R-air}/a_1} \right) \frac{L_S}{L} \quad (16)$$

The velocity of the reflected shock wave after meeting the air/gas interface is determined by:

$$w_{R-gas} = \left\{ a_3 \sqrt{\frac{\gamma_{gas} + 1}{2\gamma_{gas}} (\Pi_R - 1) + 1} \right\} - u_2' \quad (17)$$

Therefore,  $L_{gas}/L$  can be obtained based on Eq. (14-17) as a function of  $\Pi_S$  and  $\Pi_R$  for given  $PR_W$  and  $\Pi_{comb}$ .

Finally, the maximum outlet port width  $W_T$  for which TC 3 is satisfied, can be obtained by equating the time required for the primary shock wave to run through the channel ( $L/w_S$ ) plus the opening time of the outlet port ( $W_T/V$ ) with the opening time of the inlet port ( $W_3/V$ ) and the time required for the expansion wave to reach to the end of the channel:

$$\frac{W_T}{W_3} = 1 - \frac{\frac{1}{M_S} + \frac{L_{gas}}{L} \left( \frac{1}{(u_2 + a_2)/a_1} - \frac{1}{(u_2 + a_3)/a_1} \right) - \frac{1}{W_3/M_R L}}{\frac{1}{(u_2 + a_2)/a_1}} \quad (18)$$

As mentioned above, for any given  $PR_W$ ,  $W_T - W_2 \geq 0$  should be a restriction. However, a designer may prefer obtaining a value of  $W_T - W_2$  as small as possible to fulfill TC 3. The expansion wave reaches the right channel end in a different amount of time for different combinations of  $PR_W$  and  $\Pi_{comb}$ . Thus, for a desired fixed  $PR_W$  there is only one unique  $\Pi_{comb}$  that totally satisfies TC3 and vice versa. In a practical design, the rotor may incorporate various cavities (pockets) in the end plates to reduce the sensitivity to a mismatch of the various wave arrival times (Keller, 1984). These mismatches can be caused by other events such as variation in the engine load.

The following steps summarize the procedure explained above to calculate some useful design parameters that satisfy TC 1 and TC2 and evaluate TC 3 for given  $PR_W$  and  $\Pi_{comb}$ :

- 1) Simultaneously solving Eq. (4, 7, and 8) along with the normal shock wave equations calculates  $\Pi_S$  – the local pressure ratio of the primary shock.
- 2) Using  $\Pi_S$ , simultaneously solving equations Eq. (9-12)

calculates  $\Pi_R$  – the local pressure ratio of the reflected shock.

- 3) Equation (13) calculates  $W_2/W_3$  – the lower limit of the port width ratio – as a function of  $\Pi_S$  and  $\Pi_R$ .
- 4) Equation (15) along with Eq. (14) and (16-17) gives  $L_{gas}/L$  – for dimensionless gas penetration length – as a function of  $\Pi_S$  and  $\Pi_R$ .
- 5) Finally, using  $L_{gas}/L$ , Eq. (16), and Eq. (18),  $W_T/W_3$  is calculated – the preferred value and upper limit of the port width ratio, fulfilling TC 3.

The results obtained above can be used to estimate dimensions of the rotor geometry for the given engine. For example, the baseline engine ingests an air volume of about 82 liter per second ( $Q_2 = 0.082 \text{ m}^3/\text{s}$ ). The cross-section of the outlet port is  $A_2 = Q_2/u_2$ . Similarly,  $A_3 = Q_3/u_3$  gives the cross-section of the inlet port with  $Q_3$  the volume flow rate of the burned gas, which is different from the air volume flow rate. Ignoring the small mass added with the fuel, the continuity equation relates  $Q_2$  and  $Q_3$ :

$$Q_3 = \frac{\rho_2}{\rho_3} Q_2 = \frac{\rho_2}{\rho_3} \frac{\rho_2'}{\rho_2} Q_2 \quad (19)$$

where  $\rho_2/\rho_2'$  can be expressed by using the Hugoniot equation and  $\rho_3/\rho_2'$  is obtained from the ideal gas relation between regions 3 and 2':

$$\frac{\rho_3}{\rho_2'} = \frac{R_{air}}{R_{gas}} \left( \frac{T_3}{T_2'} \right)^{-1} = \frac{R_{air}}{R_{gas}} \left[ \frac{\gamma_{air} R_{air}}{\gamma_{gas} R_{gas}} \left( \frac{M_2'}{M_3} \right)^2 \right]^{-1} \quad (20)$$

The cross-section of the outlet port is typically estimated about 10% of the frontal area of the rotor (Gyarmathy, 1983), which gives  $D_{rotor}^2 = 40 A_2/\pi$ . The rotational speed is calculated from  $n = V/\pi D_{rotor}$ , where the tangential speed of the rotor  $V$  is a variable to be chosen by the designer. The channel width is calculated from  $W_{cell} = \pi D_{rotor}/N$ , where  $N$  is the number of channels for a one-row rotor, e.g. in the order of 35. For a given rotor length  $L$ , the inlet and outlet port widths are calculated from:

$$W_3 = \frac{W_3}{M_R L} M_R L = \frac{W_3}{M_R L} \frac{V}{a_1} L \quad (21)$$

where  $W_3/M_R L$  is determined by Eq. (16). Equation (13) gives the port width ratio  $W_2/W_3$ , from which the absolute value of  $W_2$  can be obtained, using  $W_3$  from Eq. (21). Assuming a rectangular cross-sectional channel, the channel height is obtained by  $H_{cell} = A_2/W_2$ , which is identical to  $H_{cell} = A_3/W_3$  due to the continuity equation used in the derivations above.

For the implementation Case A of a wave rotor into the considered baseline engine, this procedure calculates:  $D_{rotor} = 81.3 \text{ mm}$ ,  $n = 7045 \text{ rpm}$ ,  $W_{cell} = 7.3 \text{ mm}$ ,  $W_3 = 40 \text{ mm}$ ,  $W_2 = 18 \text{ mm}$ , and  $H_{cell} = 28 \text{ mm}$  for chosen  $V = 30 \text{ m/s}$  and  $L = 300 \text{ mm}$ .

Considering different rotor speeds, Fig. 9 shows the relation between dimensionless channel height  $H_{cell}/R_{rotor}$ , rotor speed  $n$ , and rotor length  $L$ , where only the region below the line  $H_{cell}/R_{rotor} = 1$  (dash point) is feasible for a practical design. In difference to the  $\Pi_{comb} = 0.98$  considered in the thermodynamic section, here the data are calculated with an adjusted  $\Pi_{comb} = 0.95$ .

## SUMMARY

A review of wave rotor applications in gas turbine engines is given. It is described how compression and expansion waves are utilized to transfer energy from the gas leaving the combustion chamber to the air entering the combustion chamber. Five different advantageous implementation cases for a four-port wave rotor into given baseline engines are considered. The compressor and turbine pressure ratios, and the turbine inlet temperatures vary in the thermodynamic calculations, according to the anticipated design objectives of the five cases. For the implementation of a wave-rotor in a 30 kW microturbine, the investigation predicts increase of the

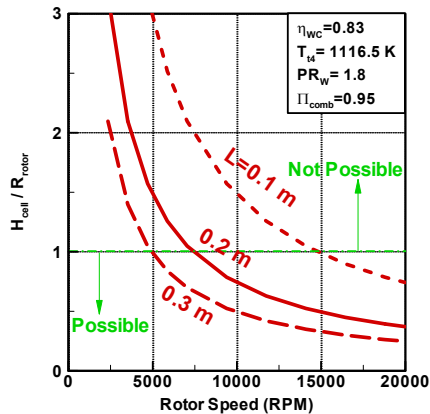


Fig. 9 Dimensionless channel height versus rotor speed and length

engine overall efficiency and specific work by up to 33%. The Gas dynamic one-dimensional model predicts the flow characteristics of the flow inside the channels and some useful design parameters such as port widths and rotor speed and size. Only tuned shock waves are considered in this work and off-tuned processes are avoided. The validity of tuning condition for the expansion wave at the channel end wall is discussed. The studies show that the wave-rotor compression ratio is one of the most important topping parameters. It links the external thermodynamics to the internal wave cycle. The wave-rotor topping allows for a higher pressure drop in the combustor, possibly reducing the size of it.

#### ACKNOWLEDGMENTS

The authors wish to acknowledge the cooperation of Capstone Turbine Corporation, providing the baseline engine data.

#### REFERENCES

- Akbari, P., Kharazi, A. A., Müller, N., 2003a, "Utilizing Wave Rotor Technology to Enhance the Turbo Compression in Power and Refrigeration Cycles," *2003 International Mechanical International Conference*, ASME Paper IMECE2003-44222, U.S.A.
- Akbari, P., and Müller, N., 2003b, "Performance Improvement of Small Gas Turbines Through Use of Wave Rotor Topping Cycles," *2003 International ASME/IGTI Turbo Exposition*, ASME Paper GT2003-38772, U.S.A.
- Akbari, P., and Müller, N., 2003c, "Gas Dynamic Design Analyses of Charging Zone for Reverse-Flow Pressure Wave Superchargers," *2003 ASME Spring Technical Conference*, ASME Paper ICES2003-690, Austria.
- Croes, N., 1978, "The Principle of the Pressure-Wave Machine as Used for Charging Diesel Engines," *Proceedings of the 11th International Symposium on Shock Tubes and Waves*.
- Fatsis A., and Ribaud Y., 1997, "Numerical Analysis of the Unsteady Flow Inside Wave Rotors Applied to Air Breathing Engines," *13th International Symposium on Airbreathing Engines*.
- Fatsis A., and Ribaud Y., 1998, "Preliminary Analysis of the Flow Inside a Three-Port Wave Rotor by Means of a Numerical Model," *Aerospace Science and Technology*, Vol. 2, No. 5, pp. 289-300.
- Fatsis A., and Ribaud Y., 1999, "Thermodynamic Analysis of Gas Turbines Topped with Wave Rotors," *Aerospace Science and Technology*, Vol. 3, No. 5, pp. 293-299.
- Gyarmathy, G., 1983, "How Does the Compress® Pressure-Wave Supercharger Work?" SAE Paper 830234.
- Jones, S. M., and Welch, G. E., 1996, "Performance Benefits for Wave Rotor-Topped Gas Turbine Engines," ASME Paper 96-GT-075.
- Keller, J. J., 1984, "Some Fundamentals of the Supercharger Compress," *Winter Annual Meeting of the ASME*, edited by Sladky, J. F., Machinery for Direct Fluid-Fluid Energy Exchange, AD-07,

pp. 47-54.

Kentfield, J. A. C., 1998, "Wave Rotors and Highlights of Their Development," AIAA Paper 98-3248.

Meyer, A., 1947, "Recent Developments in Gas Turbines," *Journal of Mechanical Engineering*, Vol. 69, No. 4, pp. 273-277.

Mayer, A., Oda, J., Kato, K., Haase, W. and Fried, R., 1989, "Extruded Ceramic - A New Technology for the Compress® Rotor," SAE Paper 890453.

Oberhem, H., and Nour Eldin, H. A., 1995, "Accurate Animation of the Thermo-Fluidic Performance of the Pressure-Wave Machine and its Balanced Material Operation," *International Journal of Numerical Methods of Heat and Fluid Flow*, Vol. 5, No. 1, pp. 63-74.

Paxson, D. E., 1993, "A Comparison Between Numerically Modeled and Experimentally Measured Loss Mechanisms in Wave Rotors," AIAA Paper 93-2522.

Paxson, D. E., 1995, "Comparison Between Numerically Modeled and Experimentally Measured Wave-Rotor Loss Mechanism," *Journal of Propulsion and Power*, Vol. 11, No. 5, pp. 908-914. See also NASA TM-106279.

Seippel, C., 1946, "Pressure Exchanger," U.S. Patent 2,399,394.

Shreeve, R. P., and Mathur, A., 1985, *Proceeding ONR/NAVAIR Wave Rotor Research and Technology Workshop*, Report NPS-67-85-008, Naval Postgraduate School, Monterey, CA.

Snyder, P. H., 1996, "Wave Rotor Demonstrator Engine Assessment," NASA CR-198496.

Snyder, P. H., and Fish, R. E., 1996, "Assessment of a Wave Rotor Topped Demonstrator Gas Turbine Engine Concept," ASME Paper 96-GT-41.

Taussig, R. T., 1984, "Wave Rotor Turbofan Engines for Aircraft," *Winter Annual Meeting of the ASME*, edited by Sladky, J. F., Machinery for Direct Fluid-Fluid Energy Exchange, AD-07, pp. 9-45.

Weber, H. E., 1995, *Shock Wave Engine Design*, John Wiley and Sons, New York.

Welch, G. E., Chima, R. V., 1993, "Two-Dimensional CFD Modeling of Wave Rotor Flow Dynamics," AIAA Paper 93-3318. See also NASA TM-106261.

Welch, G. E., Jones, S. M. and Paxson, D. E., 1995, "Wave Rotor-Enhanced Gas Turbine Engines," AIAA Paper 95-2799. See also NASA TM-106998, and ARL-TR-806.

Welch, G. E., Jones, S. M. and Paxson, D. E., 1997, "Wave Rotor-Enhanced Gas Turbine Engines," *Journal of Engineering for Gas Turbines and Power*, Vol. 119, No. 2, pp. 469-477.

Welch, G. E., 1996a, "Macroscopic Balance Model for Wave Rotors," AIAA Paper 96-0243. See also NASA TM-107114, and ARL-TR-925.

Welch, G. E., 1996b, "Two-Dimensional Computational Model for Wave Rotor Flow Dynamics," ASME Paper 96-GT-550.

Welch, G. E., 1997a, "Macroscopic Balance Model for Wave Rotors," *Journal of Propulsion and Power*, Vol. 13, No. 4, pp. 508-516.

Welch, G. E., 1997b, "Two-Dimensional Computational Model for Wave Rotor Flow Dynamics," *Journal Engineering for Gas Turbines and Power*, Vol. 119, No. 4, pp. 978-985.

Welch, G. E., 2000, "Overview of Wave-Rotor Technology for Gas Turbine Engine Topping Cycles," *Novel Aero Propulsion Systems International Symposium*, The Institution of Mechanical Engineers, pp. 2-17.

Wilson, J. and Paxson, D. E., 1993, "Jet Engine Performance Enhancement Through Use of a Wave-Rotor Topping Cycle," NASA TM-4486.

Wilson, J., Paxson, D. E., 1996, "Wave Rotor Optimization for Gas Turbine Topping Cycles," *Journal of Propulsion and Power*, Vol. 12, No. 4, pp. 778-785. See also SAE Paper 951411, 1995, and NASA TM 106951.

Zehnder, G., Mayer, A. and Mathews, L., 1989, "The Free Running Compress®," SAE Paper 890452.